Shifts in the skyrmion stabilization due to curvature effects in dome- and antidome-shaped surfaces

Vagson L. Carvalho-Santos

Departamento de Física, Universidade Federal de Viçosa, Avda. Peter Henry Rolfs s/n, 36570-000 Viçosa, MG, Brazil

R. M. Corona and D. Altbir

Departamento de Física, CEDENNA, Universidad de Santiago de Chile, Avda. Ecuador 3493, Santiago, Chile

S. Castillo-Sepúlveda

Departamento de Ingeniería, Universidad Autónoma de Chile, Avda. Pedro de Valdivia 425, Providencia, Chile

The study of curvature-induced effects on the properties of nanostructures has become a cornerstone of magnetism. However, several methodologies usually used for studying nanoscale magnetic systems present difficulties for adequately describing curvature. In this work, we present a method that allows studying, under specific conditions, curved dome/antidome surfaces using an equivalent system without curvature. From the described methodology we obtain the phase diagram between easy-normal and skyrmionic magnetization configurations, as a function of spin-orbit coupling, Dzyaloshinskii-Moriya interaction (DMI), and curvature. The effective DMI of the dome structure increases with the curvature. Nevertheless, the effective anisotropy presents the opposite behavior, decreasing with curvature. These results allow us to conclude that an increase in the skyrmion stability is observed in nanostructures having positive curvature. The presented results propose a route that could facilitate the study of curved nanofilms with intrinsic DMI from comparing them with their planar counterparts.

I. INTRODUCTION

During the past few decades, there has been a strong interest in studying the effects of geometry on the properties of nanomagnets. This interest is due to the interesting fundamental properties presented by magnetic elements at the nanoscale, as well as the potential applications they offer, such as race-track memory [1,2], nano-oscillators [3,4], shapeable magnonics [5,6], neuromorphic computation [7], magnetic field sensors for magnetofluidic applications [8,9], spin-wave filters [10,11], among others. In this context, the analysis of curvature-induced effects on the properties of nanostructures has become a cornerstone in magnetism. The remarkable development in the fabrication of nanomagnets has made possible the production of architectures of curved thin films [12] and bent nanowires [13], bringing experimental insights into the fundamental properties of three-dimensional (3D) curved objects [14]. At the same time, the theoretical study of curvature effects on the magnetization of nanostructures has revealed new emergent phenomena [15–20] of great impact from both applied and fundamental physics.

The magnetization behavior of a nanoparticle is the result of the competition between different interactions, such as exchange, dipolar, anisotropy, Zeeman, and Dzyaloshinskii-Moriya interactions (DMIs). In particular, the DMI can appear as a result of the spin-orbit (SO) effect in the breakdown of inversion symmetry either in volume or surface [21–26].

Together with other energy contributions, the magnetochirality induced by the DMI is responsible for the nucleation of stable skyrmions that propagate through magnetic stripes under the action of a small current density, making them ideal for applications in magnonic and spintronic devices [27–30]. Recently, Gaididei *et al.* [15] and Hertel [16] showed that magnetochiral effects can be driven by curvature. This curvature-induced magnetochirality (CIM) is characteristic of bent and curved wires [31–33] and curved surfaces [18,19,34]. Previous works have predicted that swirling spin textures such as vortices [35–39] can appear as magnetization ground-states on hemispherical ferromagnetic caps. Remarkably, unlike the planar case, in which the SO-driven intrinsic DMI is required for the skyrmion stabilization, the curvature-induced exchange-driven DMI is responsible for the appearance of a stable skyrmion solution on a spherical shell even when SO-driven DMI is absent [40]. Similarly, Pylypovskyi *et al.* [41] studied circular nanoindentation from mapping an arbitrary surface of revolution on a plane, obtaining coefficients for the curvature-induced exchange-driven DMI and anisotropy, and they showed that magnetic skyrmions can be stabilized in a local curvature without any intrinsic SO-driven DMI.

Following these ideas, we study the effects of the SO coupling in magnetic thin films deposited on curved substrates [37,42]. We show that under specific conditions, the SO-driven and the exchange-driven curvature-induced DMI can be linearly proportional. For our calculations, we consider dome/antidome structures that can be described by mimicking them to an equivalent planar nanostructure with effective DMI and anisotropy that depend on the geometrical parameters. From analytical calculations and micromagnetic simulations using planar nanodots, we showed that the interplay between curvature and SO-induced DMI increases (decreases) the stability of skyrmions in dome (antidome) structures.
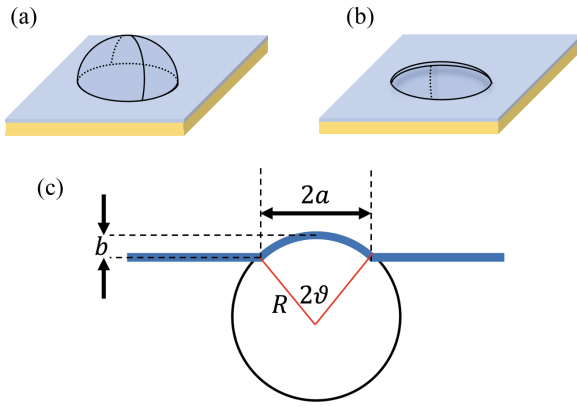
FIG. 1. Representation of (a) dome and (b) antidome. Part (c) illustrates the parameters used in our calculations

This work is divided as follows: in Sec. II we present the theoretical model that is used to determine the magnetic energy of curved structures. Section III presents the application of the theoretical model for describing the magnetization ground state of magnetic dome/antidome nanostructures. In Sec. IV we present the conclusions.

II. THEORETICAL MODEL

The system we studied consists of a single ferromagnetic surface with thickness t deposited on top of a curved heavy metal (HM) substrate, as shown in Fig. 1. The interaction between the ferromagnetic film and the HM induces a strong uniaxial anisotropy normal to the HM surface [43], and a SO coupling [44]. Both curvature and spin-orbit coupling are responsible for two contributions to the effective DM interaction: the usual SO-driven DMI (SODMI) and the exchange-driven curvature-induced DMI (ECDMI). In this context, the skyrmion stabilization can be favored or unfavored, depending on the substrate curvature. Magnetostatic contributions can be included as an extra anisotropy, as shown in Refs. [45,46]. Since a rough estimation of this extra anisotropy is of the order of 10% of the easy normal anisotropy included in our calculation, its inclusion has no qualitative effects. Therefore, and for simplicity, we neglected it.

For our calculations, we parametrized a thin ferromagnetic film as $\mathbf{X} = \mathbf{X}(u, v)$, where u and v are local curvilinear coordinates. In this context, there are two vectors, defined as $\mathbf{n}_1$ and $\mathbf{n}_2$, that represent the normals of two different oriented local bases. By considering a surface parametrized with generic coordinates $\{u, v\} = \{x^1, x^2\}$, a local orthogonal basis at each point can be described by the triad $\{\mathbf{e}_1, \mathbf{e}_2, \mathbf{e}_3\}$, where $\mathbf{e}_\alpha = \mathbf{g}_\alpha / \sqrt{g_{\alpha\alpha}}$, with $\mathbf{g}_\alpha = \partial_\alpha \mathbf{X}$, $g_{\alpha\beta} = \mathbf{g}_\alpha \cdot \mathbf{g}_\beta$, and $\alpha = (1, 2)$. In this framework, $\mathbf{e}_3 = \mathbf{e}_1 \times \mathbf{e}_2$ is the unitary vector pointing along the normal to the surface direction. From now on, we assume that the normal vectors $\mathbf{n}_1 = \mathbf{n}$ and $\mathbf{n}_2 = -\mathbf{n}$ are related to the parametrizations $\mathbf{B}_1 = \{x^1, x^2\} = \{u, v\}$ and $\mathbf{B}_2 = \{x^1, x^2\} = \{v, u\}$, respectively. Indeed, for $\mathbf{B}_1$ the local basis is $\{\mathbf{e}_u, \mathbf{e}_v, \mathbf{e}_u \times \mathbf{e}_v\}$, and for $\mathbf{B}_2$ the local basis is $\{\mathbf{e}_v, \mathbf{e}_u, -\mathbf{e}_u \times \mathbf{e}_v\}$. The main advantage of adopting these two different parametrizations is that such a local basis allows us to define the normal vector pointing in ($\mathbf{B}_1$) or out ($\mathbf{B}_2$) of the dome. That is, the dome and the antidome

can be identified by $\mathbf{B}_1$ and $\mathbf{B}_2$, respectively (see Fig. 2). As will be shown, this subtle change in the local basis can bring substantial changes in the observed behavior of the curvature-induced anisotropy and DMI. The magnetization can be parametrized as a vector field lying on the curvilinear basis, $\mathbf{m} = \sin\theta \, \cos\phi \, \mathbf{e}_1 + \sin\theta \, \sin\phi \, \mathbf{e}_2 + \cos\theta \, \mathbf{e}_3$.

The total energy density is given by $\mathcal{E} = \mathcal{E}_x + \mathcal{E}_a + \mathcal{E}_D$, where $\mathcal{E}_x$, $\mathcal{E}_a$, and $\mathcal{E}_D$ are, respectively, the exchange, anisotropy, and SO-driven DMI energy densities. From the described parametrization, the exchange energy density can be written as [15]

$$\mathcal{E}_x = \mathcal{A}[\nabla\theta - \boldsymbol{\Gamma}]^2 + \mathcal{A}\left[\sin\theta\,(\nabla\phi - \boldsymbol{\Omega}) - \cos\theta\,\frac{\partial\boldsymbol{\Gamma}}{\partial\phi}\right]^2, \tag{1}$$

where $\mathcal{A}$ is the stiffness constant, $\boldsymbol{\Gamma} = H\,\boldsymbol{\varepsilon}(\phi)$, with $H_{\alpha\beta} = (g_{\alpha\alpha}\,g_{\beta\beta})^{-1/2}(\mathbf{e}_1 \times \mathbf{e}_2)\cdot\partial_\beta\,\mathbf{g}_\alpha$, $\boldsymbol{\varepsilon}(\phi) = \cos\phi\,\mathbf{e}_1 + \sin\phi\,\mathbf{e}_2$, and $\boldsymbol{\Omega}$ is the modified spin-connection [15], which is a quantity used to define both torsion and curvature, whose components are given by $\Omega_\alpha = (g_{\alpha\alpha})^{-1/2}\mathbf{e}_1\cdot\partial_\alpha\,\mathbf{e}_2$. Additionally, the anisotropy energy density is defined as $\mathcal{E}_a = -\lambda\cos^2\theta$, where $\lambda > 0$ is the easy-normal anisotropy constant depending on the material parameters. Finally, the DMI energy density is given by [40,47]

$$\mathcal{E}_D = \mathcal{D}\boldsymbol{\varepsilon}\cdot\nabla\theta + \mathcal{D}\sin\theta\cos\theta\,\partial_\phi\,\boldsymbol{\varepsilon}\cdot(\nabla\phi - \boldsymbol{\Omega}) - \mathcal{D}\mathcal{H}\cos^2\theta, \tag{2}$$

where $\mathcal{D}$ is the DMI constant and $\mathcal{H}$ is the mean curvature. It is worthwhile to notice that Eq. (1) contains an exchange-driven curvature-induced DM term and anisotropy, while Eq. (2) evidences the appearance of an effective DMI-driven uniaxial anisotropy proportional to the mean curvature. Therefore, such curvature-induced interactions must play an important role in describing the magnetization ground state in curvilinear films.

III. SKYRMION STABILITY IN DOME/ANTIDOME STRUCTURES

Looking for the possibility of describing curved magnetic films from the study of equivalent planar structures, we rewrite the magnetic energy density coming from Eqs. (1) and (2) as $\mathcal{E} = \mathcal{E}_{\text{eff}}^x + \mathcal{E}_{\text{eff}}^a + \mathcal{E}_{\text{eff}}^D$, where

$$\mathcal{E}_{\text{eff}}^x = \mathcal{A}[(\nabla\theta)^2 + \sin^2\theta\,(\nabla\phi - \boldsymbol{\Omega})^2], \tag{3a}$$

$$\mathcal{E}_{\text{eff}}^a = \mathcal{A}[\cos^2\theta\,(\partial_\phi\,\boldsymbol{\Gamma})^2 + \boldsymbol{\Gamma}^2] - \lambda\cos^2\theta - \mathcal{D}\mathcal{H}\cos^2\theta, \tag{3b}$$

$$\mathcal{E}_{\text{eff}}^D = \boldsymbol{\xi}\cdot\nabla\theta + \sin\theta\,\cos\theta\,\partial_\phi\,\boldsymbol{\xi}\cdot(\nabla\phi - \boldsymbol{\Omega}), \tag{3c}$$

with $\boldsymbol{\xi} = \mathcal{D}\boldsymbol{\varepsilon} - 2\mathcal{A}\boldsymbol{\Gamma}$. A very interesting property appears whenever $\boldsymbol{\varepsilon}$ is proportional to $\boldsymbol{\Gamma}$, that is, when $\boldsymbol{\varepsilon} = \kappa_D\boldsymbol{\Gamma}$, where
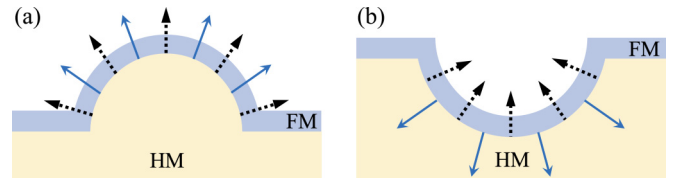

FIG. 2. Schematic representation of (a) dome and (b) antidome vector fields. Solid lines illustrate the normals to the surface, and dotted lines depict the DMI induced by SOC.

κ_D is a constant. As shown below, this proportionality occurs when there is a spherical surface. In this case, we can rewrite $\boldsymbol{\xi} = \tilde{\mathcal{D}}\boldsymbol{\varepsilon}$, where $\tilde{\mathcal{D}} = \mathcal{D} - 2\mathcal{A}\kappa_D$. Additionally, except for a constant that does not account for the energy minimization, Eq. (3b) can be rewritten as $\mathcal{E}_{\text{eff}}^u = -\tilde{\lambda}\cos^2\theta$, where $\tilde{\lambda} = \lambda - \mathcal{A}/\kappa_D^2 + D\mathcal{H}$. The condition of linear proportionality between $\boldsymbol{\varepsilon}$ and $\boldsymbol{\Gamma}$ is reached when the elements of the H matrix are $H_{\alpha\beta} = h\,\delta_{\alpha\beta}$, with h constant. We will now adopt these conditions on an arbitrary geometry with azimuthal symmetry, parametrized as $\mathbf{X} = (\varrho\cos\varphi, \varrho\sin\varphi, f(\varrho))$. In this case, we have that

$$H_{\varrho\varrho} = H_{\varphi\varphi} = h \Rightarrow \frac{f''(\varrho)}{1 + f'(\varrho)^2} = \frac{f'(\varrho)}{\varrho}, \qquad (4)$$

whose solutions are $f(\varrho) = \text{const}$ and $f(\varrho) = \sqrt{\mathcal{R}^2 - \varrho^2}$. That is, the described approximation is valid for a spherical surface with radius $\mathcal{R}$. Based on this, we will obtain the energy density associated with domelike and antidomelike structures, as shown in Fig. 1. Such structures are described by the radius of the dome/antidome basis a and the curvature radius R. Additionally, ϑ defines the zenith angle [see Fig. 1(c)]. These variables are related by $\sin\vartheta = a/R$ in such a way that the parametrization of each dome or antidome is

$$\mathbf{X}(u, v) = (R\sin(u/R)\cos v, R\sin(u/R)\sin v, \cos(u/R)), \qquad (5)$$

with $u \in [0, R\vartheta]$ and $v \in [0, 2\pi]$. Assuming two different parametrizations, $\mathbf{B}_1 = \{u, v\}$ and $\mathbf{B}_2 = \{v, u\}$, the local basis allows us to define the normal vector pointing in ($\mathbf{B}_1$) or out ($\mathbf{B}_2$) of the dome. That is, the dome and the antidome can be identified by $\mathbf{B}_1$ and $\mathbf{B}_2$, respectively (see Fig. 2).

From now on, we will consider that the magnetization profile on the dome/antidome presents a typical solution with the form $\theta = \theta(u)$ and $\phi = \phi_0$. In this case, we obtain that the normalized energy density for the dome/antidome is

$$\mathcal{E} = \mathcal{A}(\partial_u\theta)^2 + \frac{\mathcal{A}}{R^2}\sin^2\theta\,\cot^2(u/R)$$
$$+ \tilde{\mathcal{D}}^\pm\cos\phi\,[\partial_u\theta + (1/R)\sin\theta\,\cos\theta\,\cot(u/R)]$$
$$+ \frac{\mathcal{A}}{R^2} - \tilde{\lambda}^\pm\cos^2\theta, \qquad (6)$$

where

$$\tilde{\mathcal{D}}^\pm = \frac{2\mathcal{A}}{R} \pm \mathcal{D}, \quad \tilde{\lambda}^\pm = \lambda - \frac{\mathcal{A}}{R^2} \pm \frac{2\mathcal{D}}{R}. \qquad (7)$$

Here the sign $+$ $(-)$ refers to the dome (antidome) energy density. The term $\mathcal{D}_{\text{eff}}^x = 2\mathcal{A}/R$ corresponds to the ECDMI, and $\lambda^{\text{ani-exc}} = \lambda - \frac{\mathcal{A}}{R^2}$ is the effective anisotropy coming from the exchange interaction. In Fig. 3 we illustrate the ECDMI term and $\lambda^{\text{ani-exc}}$ as a function of ϑ for different values of a, which is directly related to the dome/antidome curvature. We can observe that ECDMI depends on ϑ. Indeed, we can rewrite $\mathcal{D}_{\text{eff}}^{\text{exc}} = 2\mathcal{A}/R = 2\mathcal{A}\sin\vartheta/a$, and therefore the increase in the dome curvature induces an increase in the ECDMI. This behavior is also evidenced by changing the values of the radius a. The curvature-induced anisotropy can also be represented as a function of ϑ as $\lambda_{\text{eff}}^{\text{ani-exc}} = \lambda - \frac{\mathcal{A}\sin^2\vartheta}{a^2}$, in such a way that the increase in the dome curvature induces the decrease of the effective anisotropy. The main results are
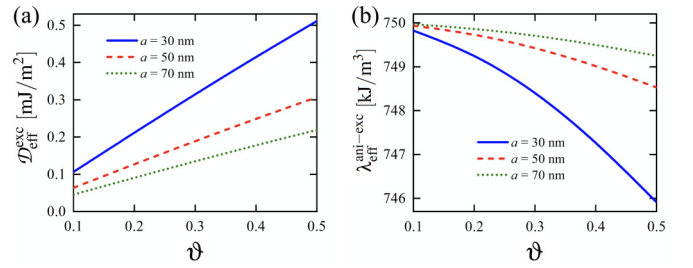

FIG. 3. (a) Exchange-driven curvature-induced DMI and (b) effective anisotropy as a function of ϑ for different values of a. Blue-solid, red-dashed, and green-dotted lines show, respectively, the obtained results for $a = 30$, 50, and 70 nm.

presented in Fig. 3(b), where we can observe that $\lambda_{\text{eff}}^{\text{ani-exc}}$ decrease with both ϑ and a. Indeed, the difference between the anisotropies of the domes is more prominent for $\vartheta = 0.5$. In this case, domes with $a = 50$ nm (red-dashed line) present a reduction of $\sim 0.04\%$ in the effective anisotropy when comparing the values for $\vartheta = 0.1$ and 0.5. On the other hand, this difference increases to $\sim 0.53\%$ when $a = 30$ nm (green-dotted line).

Now, assuming that the skyrmion radius u_0 is of the order of the characteristic length $\ell_{\text{ch}} = \sqrt{A/\lambda}$ coming from the competition between exchange and anisotropy, and that $R \geqslant 3w$, we can consider that $\cot(u/R) \to R/u$, $R\sin(u/R) \to u$, and the total energy, evaluated as $E = t\int\mathcal{E}\,da$, with $da = 2\pi R\sin(u/R)du$, can be obtained from $E = 2\pi t\int\mathcal{E}u\,du$, where the normalized energy density now reads

$$\mathcal{E} = \mathcal{A}\left[(\partial_u\theta)^2 + \frac{1}{u^2}\sin^2\theta\right] - \tilde{\lambda}^\pm\cos^2\theta$$
$$+ \tilde{\mathcal{D}}^\pm\cos\phi_0\left[\partial_u\theta + \frac{1}{u}\sin\theta\,\cos\theta\right] + \frac{\mathcal{A}}{R^2}. \qquad (8)$$

Equation (8) is equivalent to the energy of a skyrmion in a planar disk with DMI and uniaxial anisotropy constants given by $\tilde{\mathcal{D}}$ and $\tilde{\lambda}$, respectively. The corresponding planar disk radius is u, with $u \in [0, \vartheta R]$. Therefore, a dome/antidome nanomagnet can be analyzed using an equivalent magnetic disk, under the transformation

$$\mathcal{D}_d \to \frac{2\mathcal{A}}{R} \pm \mathcal{D},$$
$$\lambda_d \to \lambda - \frac{\mathcal{A}}{R^2} \pm \frac{2\mathcal{D}}{R},$$
$$u_d \to \vartheta R. \qquad (9)$$

This result allows us to conclude that skyrmions lying on a magnetic dome/antidome can be studied using a nanodisk with external radius u_d whose magnetic parameters—DMI and anisotropy—are given, respectively, by $\mathcal{D}_d$ and λ_d. Figure 4 depicts the two analyzed magnetization configurations lying in a dome with easy-normal (EN) anisotropy. For $\theta_{\text{EN}} = 0$, the magnetization describes an easy-normal configuration [see Fig. 4(a)], while $\theta_{\text{SK}} = 2\arctan(\exp(-(u_0 - u)/w))$ describes a solitonlike pattern (SK) [see Fig. 4(b)]. The parameters w and u_0 define, respectively, the profile and the radius of the soliton.
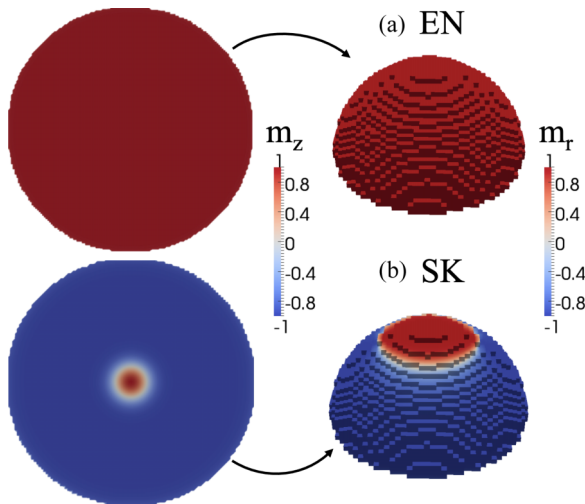
FIG. 4. Schematic representation of the magnetization profile of the radial component of the magnetization in a dome. (a) An easy-normal (EN) configuration and (b) a soliton (SK) configuration.

Aiming at showing that the presented analytical model can describe a dome with magnetic parameters given by $\mathcal{D}$ and λ from considering a disk having magnetic parameters $\mathcal{D}_d$ and λ_d, we obtain the energy gap between EN the SK excited state in both structures. From considering a high easy-normal anisotropy constant, $\lambda \geqslant 10^6$ J/m^3, the magnetization ground state of both nanodisk and nanodome are given by θ_{EN}. That is, the lower energy state is described by an EN. The energy gap between EN and SK for both structures is presented in Fig. 5, which illustrates the energy density difference $\Delta\varepsilon = \varepsilon(\theta_{\mathrm{SK}}) - \varepsilon(\theta_{\mathrm{EN}})$ as a function of u for a dome (red dotted line) and for a disk (black solid line). In those figures, $\varepsilon(\theta_{\mathrm{SK}})$ and $\varepsilon(\theta_{\mathrm{EN}})$ are the energy densities for the easy-normal and soliton configurations, respectively. For the dome, we define $\varepsilon = 2\pi Rt\,\mathcal{E}\sin u/R$, and for the disk, we define $\varepsilon = 2\pi t\,\mathcal{E}u$. For small values of u_0 (small soliton radius), we observe that $\Delta\varepsilon$ is practically equal for both disk and dome, in such a way that both geometries should present the same stable and metastable magnetization configurations. For large values of u_0 (large soliton radius), the energy density difference for a disk, $\Delta\varepsilon_{\mathrm{disk}}$, is lower than the energy density difference of a dome structure, $\Delta\varepsilon_{\mathrm{dome}}$. For instance, for $u_0 = 45$ nm, $(\Delta\varepsilon_{\mathrm{disk}} - \Delta\varepsilon_{\mathrm{dome}}) \times 100\%/\Delta\varepsilon_{\mathrm{disk}} \approx 13\%$ [see Fig. 5(b)]. In this case, for large u_0 values, the proposed methodology proposed is not strictly valid. Nevertheless, since the radius
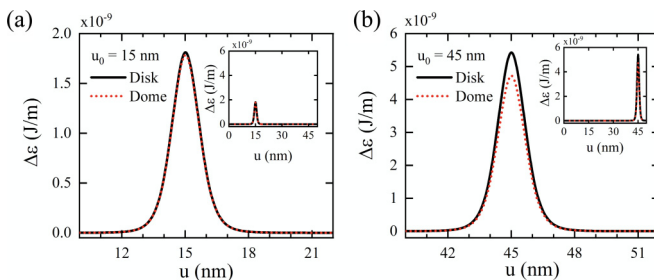
of solitons induced by SOC are in the order of 15 nm, our model can be used in a large range of applications.

The range of validity of our model allows us to use the equivalence previously described to obtain the phase diagram of curved surfaces using micromagnetic simulations with the MUMAX3 [48] public software. We have then performed micromagnetic simulations to obtain stable states in a planar disk having effective exchange, anisotropy, and DMI constants given by the set of Eqs. (7). Therefore, the simulated structure consists in a straight disk that by changing energy strengths represents a dome described by the geometrical parameters a, R, and ϑ related by $\sin\vartheta = a/R$ (see Fig. 1). For our simulations we use the exchange stiffness $\mathcal{A} = 16$ pJ/m, saturation magnetization $M_s = 1.1$ MJ/m^3, a damping parameter $\alpha = 0.1$, and perpendicular anisotropy magnetization $\lambda = 0.75$ MJ/m^3. These parameters correspond to the system described in a previous work [49]. For our calculations, we vary the DMI constant between 0.0 and 3.5 mJ/m^2. The initial state consists in a soliton at the center of the disk, and we relax the magnetization in a disk with radius ϑR and parameters $\mathcal{D}_d$ and λ_d that, according to our previous calculations, represent a dome with magnetic parameters $\mathcal{D}$ and λ, and geometric parameters ϑ and $a = R\sin\vartheta$. The considered parameters yield an EN as the lower energy state, as illustrated in Fig. 4(a). However, due to the topological protection of skyrmions, our simulations revealed that solitonlike configuration can appear as a metastable state in the considered structures, depending on the geometrical parameters.

From our calculations, we obtain the phase diagram presenting the magnetization relaxed states with $a = 30$, 50, and 70 nm (see Fig. 6). To obtain such a phase diagram, we allow the magnetization to relax from an initial configuration suitable to reach solitonlike configurations. Black triangles correspond to states with an easy-normal (EN) configuration, while red dots represent skyrmion (SK) states. The ground state has been obtained as a function of $\mathcal{D}_{\mathrm{eff}}^{\pm}$ and ϑ, where the considered dots have radius ϑR, where $\vartheta \in [0.1, 0.5]$. We have performed the micromagnetic simulations describing the dome structures. The solutions for the antidome were obtained from the transformations $\theta^- = \theta^+ + \pi$ and $\phi^- = -\phi^+ - \pi/2$. The main results are presented in Fig. 6, in which we show the transition line separating the EN and SK states as a function of the SODMI and curvature. Due to the appearance of an ECDMI, the value of SODMI that stabilizes the skyrmion decreases. Indeed, from Fig. 6(a) we observe that a decrease of a increases the skyrmion stabilization in such a way that for very small values of a (large curvature), the skyrmion can be stabilized even if there is no SODMI. This result agrees with the obtained in Ref. [40], in which the authors showed that when the radius of the sphere is larger than $2w$, hedgehog-like magnetization configurations are stabilized in this geometry. Nevertheless, a different behavior occurs when we analyze the magnetization ground state of an antidome. In this case, because SODMI is subtracted in the effective DMI [see Eq. (7)], there is a competition between SODMI and ECDMI in such a way that the soliton state appears only for SODMI values larger than a critical value given by $\mathcal{D}_{\mathrm{crit}} > \mathcal{D}$. Aiming at showing that the obtained results from micromagnetic simulations in nanodisks effectively describe the relaxed states of magnetic nanodomes, we determine the radii of the
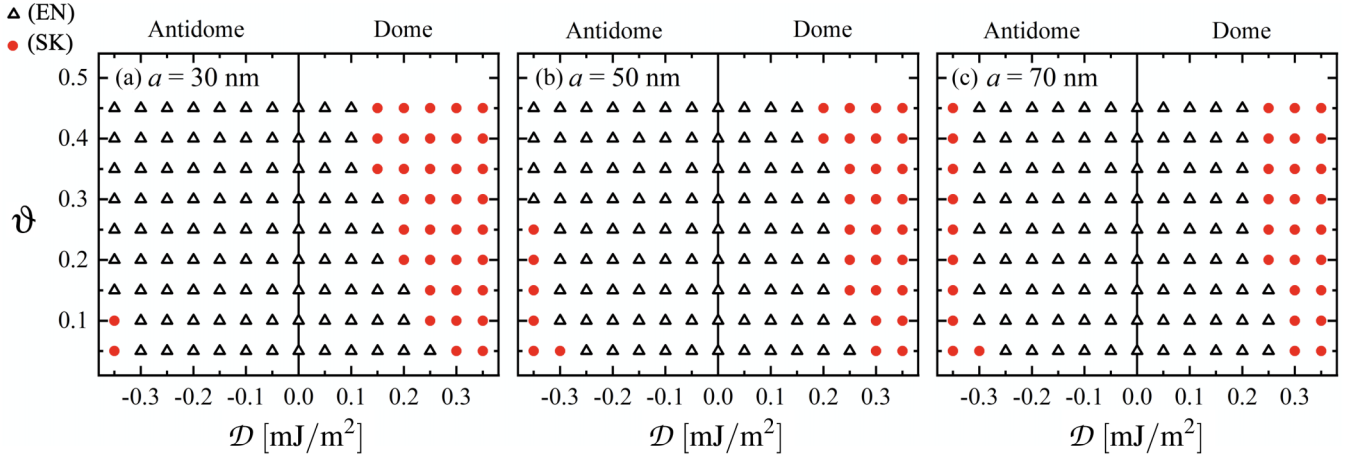

FIG. 5. $\Delta\varepsilon$ as a function of u for a dome and for a disk (a) for $u_0 = 15$ nm and (b) for $u_0 = 45$ nm.

FIG. 6. Phase diagram (ϑ, $\mathcal{D}$) for a dome (right side) and an antidome (left side) for different a values. Black triangles depict states with an easy-normal (EN) configuration, while red dots represent skyrmion (SK) states.

relaxed SK states. Because the obtained skyrmion radii are in the range of $u_0 \leqslant 15$ nm, we can state that in the range of the studied systems, $(\Delta\varepsilon_{\text{disk}} - \Delta\varepsilon_{\text{dome}}) \times 100\%/\Delta\varepsilon_{\text{disk}} \leqslant 1.5\%$ [see Fig. 5(a)]. In this context, we can state that both methods (analytical and micromagnetic calculations) are equivalent.

IV. CONCLUSIONS

Using a theoretical model, we performed an analysis of the curvature-induced DMI and anisotropy for curved structures with azimuthal symmetry. Our results evidence that the dome/antidome geometries can be addressed as a noncurved disk when spin-orbit-driven and exchange-driven DM interactions are linearly proportional. We then analyzed the energy density describing magnetic dome and antidome shells, and we obtained the curvature-induced DMI and the anisotropy as a function of the curvature. The dome structure presents an increase in the effective DMI when the curvature increases. Nevertheless, the effective anisotropy presents the opposite behavior, decreasing with curvature. The

obtained results suggest that, for some specific conditions regarding the skyrmion width, the magnetic ground-state for dome/antidome nanoshells can be obtained by analyzing a planar disk with DMI and anisotropy constants changed by factors depending on the curvature. Using these transformations, we obtained the phase diagram for the easy-normal and skyrmion magnetization configurations as a function of the spin-orbit coupling DMI and curvature. This result allows us to conclude that the presence of curvature increases skyrmion stability. Our results propose a route that could facilitate the study of curved nanofilms with intrinsic DMI.

ACKNOWLEDGMENTS

APPENDIX: FIELD TRANSFORMATIONS

The field transformations $\theta^- = \theta^+ + \pi$ and $\phi^- = -\phi^+ - \pi/2$ were obtained in the following way:

$$\mathbf{m}_1 = \sin\theta_1\cos\phi_1\mathbf{e}_u + \sin\theta_1\sin\phi_1\mathbf{e}_v + \cos\theta_1\mathbf{e}_u \times \mathbf{e}_v$$
$$\mathbf{m}_2 = \sin\theta_2\cos\phi_2\mathbf{e}_v + \sin\theta_2\sin\phi_2\mathbf{e}_u + \cos\theta_1\mathbf{e}_v \times \mathbf{e}_u$$

$$\Rightarrow \begin{aligned} \sin\theta_1\cos\phi_1 &= \sin\theta_2\sin\phi_2 \\ \sin\theta_1\sin\phi_1 &= \sin\theta_2\cos\phi_2 \\ \cos\theta_1 &= -\cos\theta_2, \end{aligned} \tag{A1}$$

where $\mathbf{m}_1$ is for the parametrization $\mathbf{B}_1$, and $\mathbf{m}_2$ is for the parametrization $\mathbf{B}_2$.

If we consider that $\mathbf{e}_u \cdot \mathbf{e}_v = \delta_{uv}$, we obtain

$$\nabla_u(\delta_{uv}) = \nabla_u(\mathbf{e}_u \cdot \mathbf{e}_v) \Rightarrow 0 = (\nabla_u\mathbf{e}_u) \cdot \mathbf{e}_v + \mathbf{e}_u \cdot (\nabla_u\mathbf{e}_v) = \Omega_1^{(1)} + \Omega_2^{(2)} = 0, \tag{A2}$$

$$\nabla_v(\delta_{uv}) = \nabla_v(\mathbf{e}_u \cdot \mathbf{e}_v) \Rightarrow 0 = (\nabla_v\mathbf{e}_u) \cdot \mathbf{e}_v + \mathbf{e}_u \cdot (\nabla_v\mathbf{e}_v) = \Omega_2^{(1)} + \Omega_1^{(2)} = 0. \tag{A3}$$

The above result implies that under the transformations $\theta^- = \theta^+ + \pi$ and $\phi^- = -\phi^+ - \pi/2$, the modified spin-connections are related by $\Omega_1^{(1)} = -\Omega_2^{(2)}$ and $\Omega_2^{(1)} = -\Omega_1^{(2)}$.

From defining $\mathcal{X}_{\alpha\beta}^{(3)} = (\mathbf{e}_u \times \mathbf{e}_v) \cdot \partial_\beta \mathbf{X}_\alpha / \sqrt{g_{\alpha\alpha} g_{\beta\beta}}$, and considering that $\mathcal{X}_{uv}^{(3)} = \mathcal{X}_{vu}^{(3)} = 0$, we obtain that the matrix $\mathbf{H}$ elements are given by

$$H^{(1)} = \begin{pmatrix} \mathcal{X}_{uu}^{(3)} & 0 \\ 0 & \mathcal{X}_{vv}^{(3)} \end{pmatrix}, \tag{A4}$$

$$H^{(2)} = \begin{pmatrix} -\mathcal{X}_{vv}^{(3)} & 0 \\ 0 & -\mathcal{X}_{uu}^{(3)} \end{pmatrix}. \tag{A5}$$

If we define $\mathcal{T}$ with $\mathcal{T}_{11} = \mathcal{T}_{22} = 0$ and $\mathcal{T}_{12} = \mathcal{T}_{21} = -1$, we have that $\Omega_\alpha^{(1)} = \mathcal{T}_{\alpha\beta} \Omega_\beta^{(2)}$ and $H_{\alpha\beta}^{(1)} = \mathcal{T}_{\alpha\gamma} H_{\gamma\beta}^{(2)}$.

In this context, using the described transformation for fields, we can obtain that the energy (1) is invariant under the transformations $\theta^- = \theta^+ + \pi$ and $\phi^- = -\phi^+ - \pi/2$, since the DMI term for the energy is replaced as follows: $\mathcal{D} \to -\mathcal{D}$.

[1] S. S. P. Parkin, M. Hayashi, and L. Thomas, Science **320**, 190 (2008).

[2] S. Parkin and S.-H. Yang, Nat. Nano. **10**, 195 (2015).

[3] J. S. Moodera, L. R. Kinder, T. M. Wong, and R. Meservey, Phys. Rev. Lett. **74**, 3273 (1995).

[4] N. Perrissin, G. Gregoire, S. Lequeux, L. Tillie, N. Strelkov, S. Auffret, L. D. Buda-Prejbeanu, R. C. Sousa, L. Vila, and B. Dieny, J. Phys. D **52**, 234001 (2019).

[5] K. V. Yershov, V. P. Kravchuk, D. D. Sheka, J. van den Brink, and Y. Gaididei, Phys. Rev. B **100**, 140407(R) (2019).

[6] Y. Gaididei, K. V. Yershov, D. D. Sheka, V. P. Kravchuk, and A. Saxena, Phys. Rev. B **99**, 014404 (2019).

[7] J. Torrejon, M. Riou, F. A. Araujo, S. Tsunegi, G. Khalsa, D. Querlioz, P. Bortolotti, V. Cros, K. Yakushiji, and A. Fukushima, Nature (London) **547**, 428 (2017).

[8] I. Mönch, D. Makarov, R. Koseva, L. Baraban, D. Karnaushenko, C. Kaiser, K. F. Arndt, and O. G. Schmidt, ACS Nano **5**, 7436 (2011).

[9] C. Müller, C. C. Bof Bufon, M. E. Navarro Fuentes, D. Makarov, D. H. Mosca, and O. G. Schmidt, Appl. Phys. Lett. **100**, 022409 (2012).

[10] F. Balhorn, S. Mansfeld, A. Krohn, J. Topp, W. Hansen, D. Heitmann, and S. Mendach, Phys. Rev. Lett. **104**, 037205 (2010).

[11] F. Balhorn, S. Jeni, W. Hansen, D. Heitmann, and S. Mendach, Appl. Phys. Lett. **100**, 222402 (2012).

[12] D. Ruffer, R. Huber, P. Berberich, S. Albert, E. Russo-Averchi, M. Heiss, J. Arbiol, A. F. i Morral, and D. Grundler, Nanoscale **4**, 4989 (2012).

[13] M. P. Proenca, C. T. Sousa, J. Escrig, J. Venture, and M. Vazquez, J. Appl. Phys. **113**, 093907 (2013).

[14] R. Streubel, P. Fischer, F. Kronast, V. P. Kravchuk, D. D. Sheka, Y. Gaididei, O. G. Schmidt, and D. Makarov, J. Phys. D **49**, 363001 (2016).

[15] Y. Gaididei, V. P. Kravchuk, and D. D. Sheka, Phys. Rev. Lett. **112**, 257203 (2014).

[16] R. Hertel, SPIN **3**, 1340009 (2013).

[17] P. Landeros and Á. S. Núñez, J. Appl. Phys. **108**, 033917 (2010).

[18] S. Vojkovic, V. L. Carvalho-Santos, J. M. Fonseca, and A. S. Nunez, J. Appl. Phys. **121**, 113906 (2017).

[19] R. G. Elias, N. Vidal-Silva, and V. L. Carvalho-Santos, Sci. Rep. **9**, 14309 (2019).

[20] J. A. Otálora, M. Yan, H. Schultheiss, R. Hertel, and A. Kákay, Phys. Rev. Lett. **117**, 227203 (2016).

[21] A. N. Bogdanov and A. Hubert, J. Magn. Magn. Mater. **138**, 255 (1994).

[22] A. Crepieux and C. Lacroix, J. Magn. Magn. Mater. **182**, 341 (1998).

[23] U. K. Roßler, A. N. Bogdanov, and C. Pfleiderer, Nature (London) **442**, 797 (2006).

[24] J.-H. Han, J. Zang, Z. Yang, J.-H. Park, and N. Nagaosa, Phys. Rev. B **82**, 094429 (2010).

[25] C. Moreau-Luchaire, C. Moutafis, N. Reyren, J. Sampaio, C. A. F. Vaz, N. Van Horne, K. Bouzehouane, K. Garcia, C. Deranlot, P. Warncke, P. Wohlhuter, J.-M. George, M. Weigand, J. Raabe, V. Cros, and A. Fert, Nat. Nanotechnol. **11**, 444 (2016).

[26] J. Muller, New J. Phys. **19**, 025002 (2017).

[27] N. Nagaosa and Y. Tokura, Nat. Nanotechnol. **8**, 899 (2013).

[28] J. Sampaio, V. Cross, S. Rohart, A. Thiaville, and A. Fert, Nat. Nanotechnol. **8**, 839 (2013).

[29] X. Z. Yu, N. Kanazawa, W. Z. Zhang, T. Nagai, T. Hara, K. Kimoto, Y. Matsui, Y. Onose, and Y. Tokura, Nat. Commun. **3**, 988 (2012).

[30] C. Jin, C. Song, J. Wang, and Q. Liu, Appl. Phys. Lett. **109**, 182404 (2016).

[31] K. V. Yershov, V. P. Kravchuk, D. D. Sheka, and Y. Gaididei, Phys. Rev. B **92**, 104412 (2015).

[32] O. V. Pylypovskyi, D. D. Sheka, V. P. Kravchuk, K. V. Yershov, D. Makarov, and Y. Gaididei, Sci. Rep. **6**, 23316 (2016).

[33] R. Moreno, V. L. Carvalho-Santos, A. P. Espejo, D. Laroze, O. Chubykalo-Fesenko, and D. Altbir, Phys. Rev. B **96**, 184401 (2017).

[34] O. V. Pylypovskyi, V. P. Kravchuk, D. D. Sheka, D. Makarov, O. G. Schmidt, and Y. Gaididei, Phys. Rev. Lett. **114**, 197204 (2015).

[35] A. M. Abdelgawad, N. Nambiar, M. Bapna, H. Chen, and S. A. Majetich, AIP Adv. **8**, 056321 (2018).

[36] R. Streubel, F. Kronast, C. F. Reiche, T. Mühl, A. U. B. Wolter, O. G. Schmidt, and D. Makarov, Appl. Phys. Lett. **108**, 042407 (2016).

[37] R. Streubel, V. P. Kravchuk, D. D. Sheka, D. Makarov, F. Kronast, O. G. Schmidt, and Y. Gaididei, Appl. Phys. Lett. **101**, 132419 (2012).

[38] V. P. Kravchuk, D. D. Sheka, R. Streubel, D. Makarov, O. G. Schmidt, and Y. Gaididei, Phys. Rev. B **85**, 144433 (2012).

[39] C. I. L. Araujo, J. M. Fonseca, J. P. Sinnecker, R. G. Delatorre, N. Garcia, and A. A. Pasa, J. Appl. Phys. **116**, 183906 (2014).

[40] V. P. Kravchuk, U. K. Rößler, O. M. Volkov, D. D. Sheka, J. van den Brink, D. Makarov, H. Fuchs, H. Fangohr, and Y. Gaididei, Phys. Rev. B **94**, 144402 (2016).

[41] O. V. Pylypovskyi, D. Makarov, V. P. Kravchuk, Y. Gaididei, A. Saxena, and D. D. Sheka, Phys. Rev. Appl. **10**, 064057 (2018).

[42] D. Mitin, D. Nissen, P. Schadlich, S. S. P. K. Arekapudi, and M. Albrecht, J. Appl. Phys. **115**, 63906 (2014).

[43] J. Chon, N.-H. Kim, S. Lee, J.-S. Kim, R. Lavrijsen, A. Solignac, Y. Yin, D.-S. Han, N. J. J. van Hoof, H. J. M. Swagten, B. Koopmans, and C.-Y. You, Nat. Commun. **6**, 7635 (2015).

[44] S. Tacchi, R. E. Troncoso, M. Ahlberg, G. Gubbiotti, M. Madami, J. Akerman, and P. Landeros, Phys. Rev. Lett. **118**, 147201 (2017).

[45] R. V. Kohn and V. V. Slastikov, Arch. Ration. Mech. Anal. **178**, 227 (2005).

[46] V. V. Slastikov and C. Sonnenberg, IMA J. Appl. Math. **77**, 220 (2012).

[47] V. P. Kravchuk, D. D. Sheka, A. Kákay, O. M. Volkov, U. K. Rößler, J. van den Brink, D. Makarov, and Y. Gaididei, Phys. Rev. Lett. **120**, 067201 (2018).

[48] A. Vansteenkiste, J. Leliaert, M. Dvornik, M. Helsen, F. Garcia-Sanchez, and B. Van Waeyenberge, AIP Adv. **4**, 107133 (2014).

[49] S. Castillo-Sepulveda, R. M. Corona, A. S. Nunez, and D. Altbir, J. Magn. Magn. Mater. **484**, 451 (2019).